scientific reports

Check for updates

OPEN

Linear magnetoelastic coupling and magnetic phase diagrams of the buckled-kagomé antiferromagnet $Cu_3Bi(SeO_3)_2O_2Cl$

S. Spachmann[1]✉, P. Berdonosov[2,3], M. Markina[2], A. Vasiliev[2,3] & R. Klingeler[1]

Single crystals of $Cu_3Bi(SeO_3)_2O_2Cl$ were investigated using high-resolution capacitance dilatometry in magnetic fields up to 15 T. Pronounced magnetoelastic coupling is found upon evolution of long-range antiferromagnetic order at $T_N = 26.4(3)$ K. Grüneisen analysis reveals moderate effects of uniaxial pressure on T_N, of 1.8(4) K/GPa, −0.62(15) K/GPa and 0.33(10) K/GPa for $p \parallel a$, b, and c, respectively. Below 22 K Grüneisen scaling fails which implies the presence of competing interactions. The structural phase transition at $T_S = 120.7(5)$ K is much more sensitive to uniaxial pressure than T_N, with strong effects of up to 27(3) K/GPa ($p \parallel c$). Magnetostriction and magnetization measurements reveal a linear magnetoelastic coupling for $B \parallel c$ below T_N, as well as a mixed phase behavior above the tricritical point around 0.4 T. An analysis of the critical behavior in zero-field points to three-dimensional (3D) Ising-like magnetic ordering. In addition, the magnetic phase diagrams for fields along the main crystalline axes are reported.

Frustrated magnetism has been a highly active research field in the past three decades[1]. Besides simple corner-sharing triangular lattice geometries, the Kagomé, pyrochlore, and hyperkagome lattices offer potential playgrounds of strongly geometrically frustrated magnetism[2–4]. Among them, the ideal $S = 1/2$ Kagomé Heisenberg antiferromagnet is the most prominent realization of a system in which macroscopic ground state degeneracies, i.e., a (quantum) spin liquid state, are expected to prevent the evolution of any long-range order[5]. Other phenomena of frustrated magnetism include fractionalized magnetization plateaus, chiral and helical spin arrangements, as well as spin glass, spin nematic, and spin ice behaviors[1]. A number of geometrically frustrated systems such as $FeTe_2O_5Cl$[6], $PbCu_3TeO_7$[7], and $Ni_3V_2O_8$[8,9] were found to additionally exhibit multiferroic behavior. From a technological perspective multiferroics – materials combining more than one ferroic property such as ferromagnetism, ferroelectricity and ferroelasticity[10,11] – are especially sought-after for the control of magnetism via electric fields, with the promise of substantially lower energy consumption than manipulating magnetic states via magnetic fields[12]. Potential applications range from ultra-low power logic-memory[13] to radio- and high-frequency devices, including electric field-tunable radio-frequency/microwave signal processing, magnetic field sensors, magnetoelectric random access memory (MERAM)[14] and voltage-tunable magnetoresistance[15,16].

$Cu_3Bi(SeO_3)_2O_2Cl$, eponym of the francisite family[17–22], crystallizes in a special buckled realization of the Kagomé lattice[23] and exhibits multiferroic properties at low temperatures[24,25]. Cu^{2+} ions ($3d^9$, $S = 1/2$) situated at two different crystal sites, Cu1 and Cu2, are the magnetic centers forming the Kagomé lattice in the *ab* plane. Both Cu1 and Cu2 ions are found in a square planar coordination with Cu-O bond lengths of 1.933 Å to 1.978 Å. These plaquettes around Cu1 and Cu2 sites are non-parallel with respect to each other. Along the *c* axis Cu ions are connected by long Bi–O bonds with a bond length of about 2.8 Å. Below $T_N \approx 26$ K $Cu_3Bi(SeO_3)_2O_2Cl$ (in short: CBSCl) develops an A-type antiferromagnetic order along the *c* axis of spins aligned ferromagnetically (FM) in the *ab* plane. Cu2 spins are aligned strictly (anti)parallel with the *c* axis whereas Cu1 spins are canted towards the *b* axis by 59(4)°[25]. This peculiar magnetic order arises from the competition of large FM nearest neighbor exchange interactions (J_1 and J_1', see Fig. S2[26]) on the order of −70 K to −80 K and AFM next-nearest neighbor interactions (J_2) on the order of 60 K, in conjunction with small exchange couplings along the *c* direction ($J_{\perp,1}$ and $J_{\perp,2}$, $|J_{\perp,i}| \leq 2$ K), Dzyaloshinskii-Moriya interactions and a symmetric anisotropic exchange component[25–27]. Furthermore, a linear magnetoelectric coupling has been observed below T_N[24,25]. At higher

[1]Kirchhoff Institute for Physics, Heidelberg University, D-69120 Heidelberg, Germany. [2]Lomonosov Moscow State University, Moscow 119991, Russia. [3]National University of Science and Technology "MISiS", Moscow 119049, Russia. ✉email: sven.spachmann@kip.uni-heidelberg.de

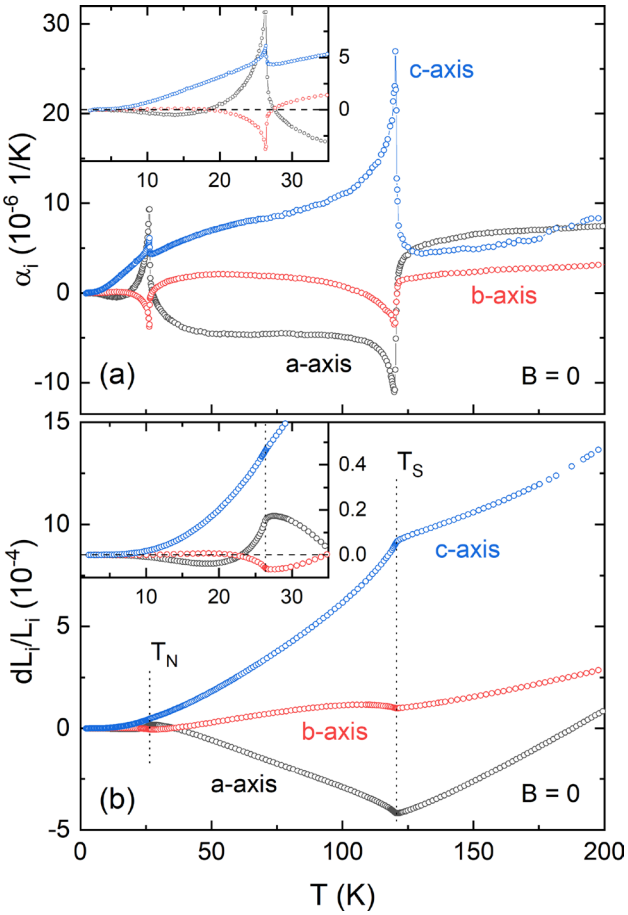

Figure 1. Zero-field thermal expansion: (**a**) Thermal expansion coefficients α_i and (**b**) relative length changes dL_i/L_i in zero-field for the crystallographic *a*, *b*, and *c* axis of CBSCl. Insets show a magnification of the low temperature regime around T_N with zero y-values indicated by horizontal dashed lines. Vertical dotted lines in (**b**) mark T_N and T_S.

temperatures around 120 K a structural phase transition from an orthorhombic *Pmmn* to an orthorhombic and nonpolar, possibly antiferroelectric (AFE), *Pcmn* space group occurs upon cooling[25,28,29].

In this paper we investigate the interplay of the lattice and spin degrees of freedom in CBSCl with high-resolution thermal expansion and magnetostriction as well as magnetization measurements. From these measurements we construct the complete magnetic phase diagram for the first time, and quantify the magnetoelastic coupling by the effects of uniaxial pressure on the phase boundaries. Furthermore, magnetostriction and magnetization measurements reveal a linear magnetoelastic coupling below T_N. Finally, a critical scaling analysis suggests that three-dimensional Ising-like magnetic ordering occurs at T_N, whereas magnetic correlations above T_N are constrained to the *ab* plane.

Results and discussion

Thermal expansion. *Zero-field.* Thermal expansion measurements in zero field show pronounced anomalies at $T_N = 26.4(3)$ K and $T_S = 120.7(5)$ K (Fig. 1).T_N these anomalies provide evidence for the presence of significant magnetoelastic coupling in CBSCl. In the thermal expansion coefficients α_i the anomalies have λ -like shapes, signaling continuous phase transitions at both T_N and T_S. Notably, the transition at T_S shows a jump superimposing the λ-like behavior for the *a* and *c* axis, but not for the *b* axis. The length changes observed in CBSCl (Fig. 1b) are highly anisotropic. While the *a* axis shrinks above T_N upon warming up to T_S, the *c* axis strongly expands in this temperature regime. Expansion along the *b* axis, in contrast, is much smaller than for the other two axes. The volume expansion is positive in the whole measured temperature regime (see supplement, Fig. S3).

Grüneisen analysis. The magnetoelastic coupling in CBSCl can be quantified by means of the uniaxial pressure dependence of T_N. This pressure dependence may be derived from the magnetic contributions to thermal expansion and specific heat using the Ehrenfest relation which is valid for continuous phase transitions[30,31]:

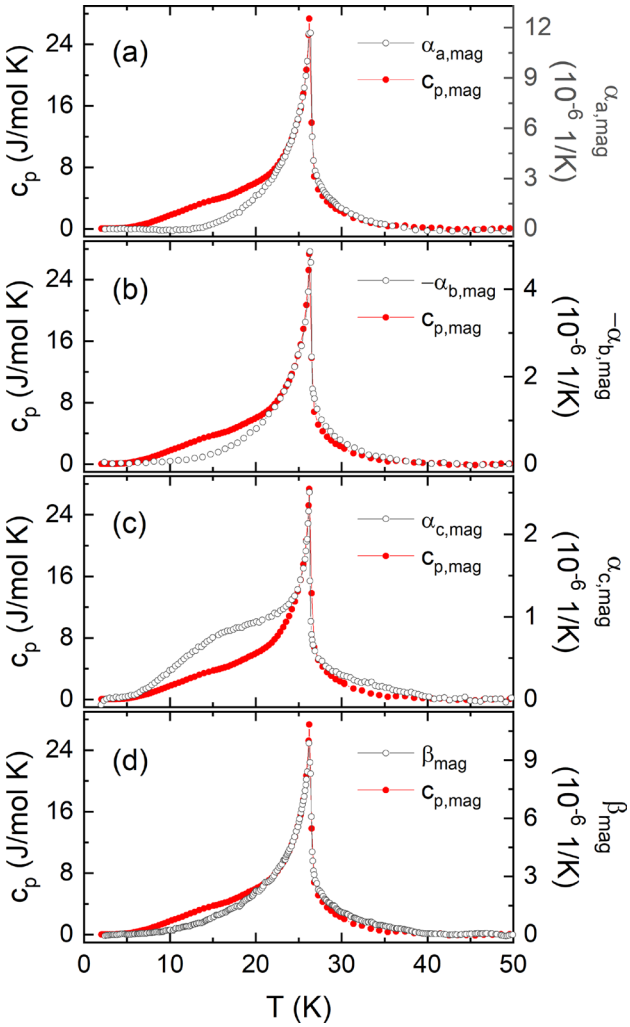

Figure 2. Grüneisen Scaling: Comparison of magnetic contributions to the specific heat (red circles, left axes) and thermal expansion (empty black circles, right axes) along the (**a**) *a* axis, (**b**) *b* axis, (**c**) *c* axis, and (**d**) for the volume expansion.

$$\frac{\partial T_N}{\partial p_i} = T_N V_m \gamma_{(mag)} = T_N V_m \frac{\alpha_{i(,mag)}}{c_{p(,mag)}}. \tag{1}$$

$\gamma_{(mag)}$ is the (magnetic) Grüneisen ratio and V_m the molar volume, which for CBSCl is $V_m = 1.333 \cdot 10^{-4}$ m^3/mol[32]. The magnetic contributions to the thermal expansion, $\alpha_{i,mag}$, and specific heat, $c_{p,mag}$, in Fig. 2 were obtained by subtracting a phononic background (see supplement, Fig. S4) estimated by a sum of Debye and Einstein functions (for more details see supplement). In order to assess the validity of a constant $\gamma_{(mag)}$ in Eq. (1), in Fig. 2 the ordinates are scaled for an optimal overlap of $\alpha_{i,mag}$ and $c_{p,mag}$ around T_N. Above T_N and down to about 22 K (24 K for *c*) the data scale well within the experimental errors which implies a single dominating energy scale in this temperature regime[30]. Below 22 K, however, a difference in the behavior of $\alpha_{i,mag}$ and $c_{p,mag}$ is clearly visible for all axes as well as the volume. This difference indicates competing interactions arising below T_N. A discussion of possible sources for this behavior is given in the supplemental material.

The magnetic Grüneisen ratio in Eq. (1) is obtained from the ratio of the scaled ordinates in Fig. 2. This results in $\gamma_{a,mag} = 5.0 \cdot 10^{-7}$ mol/J, $\gamma_{b,mag} = -1.8 \cdot 10^{-7}$ mol/J, and $\gamma_{c,mag} = 9.3 \cdot 10^{-8}$ mol/J, which yields uniaxial pressure dependencies at T_N of 1.8(4) K/GPa ($p \parallel a$), −0.62(15) K/GPa ($p \parallel b$) and 0.33(10) K/GPa ($p \parallel c$). Long-range antiferromagnetic (AFM) order is thus strengthened by pressure $p \parallel a$ and *c* whereas $p \parallel b$ influences the competition of interactions in a way that long-range order is suppressed. From a qualitative point of view, increase of T_N upon in-plane pressure which likely increases the lattice spacing along the *c* direction suggests that the perpendicular exchange couplings ($J_\perp$) are not crucially driving long-range AFM order. We also speculate that uniaxial pressure $p \parallel a$ ($p \parallel b$) changes the Cu1-O-Cu1 bond angle further towards (away from) 90°, thereby increasing (decreasing) ferromagnetic exchange J_1 while J_1' becomes smaller for $p \parallel a$. Our results, i.e., $\partial T_N/\partial p_a > 0$ and $\partial T_N/\partial p_b < 0$ hence indicate a crucial role of J_1 for stabilizing A-type AFM order.

	$\gamma_{i,\mathrm{mag}}$	$\partial T_N/\partial p_i$	γ_i	$\partial T_S/\partial p_i$
	(10^{-7} mol/J)	(K/GPa)	(10^{-7} mol/J)	(K/GPa)
a axis	5.0	1.8±0.4	−11.9	−19±6
b axis	−1.8	−0.62±0.15	−3.5	−5.7±1.1
c axis	0.93	0.33±0.10	16.9	27±3
volume	4.0	1.4±0.3	–	2.3±1.0

Table 1. Pressure dependencies of the transition temperatures calculated from the magnetic Grüneisen ratios $\gamma_{i,\mathrm{mag}}$ at T_N, as well as from the jumps $\Delta\alpha_i$ and Δc_p at T_S, for the three main crystallographic axes. The hydrostatic pressure dependence dT_S/dp is calculated as the sum of all three uniaxial ones and denoted as "volume".

The analysis of the structural phase transition yields much larger values for the uniaxial pressure dependencies $\partial T_S/\partial p_i$ in comparison with $\partial T_N/\partial p_i$. In-plane pressure strongly suppresses the structural phase transition ($\partial T_S/\partial p_a = -19(6)$ K/GPa, $\partial T_S/\partial p_b = -5.7(1.1)$ K/GPa) whereas pressure applied out-of-plane enhances T_S even more strongly ($\partial T_S/\partial p_c = 27$ K/GPa). The Grüneisen ratios corresponding to these values are derived in a different manner than for T_N, by area-conserving – and for c_p entropy-conserving – interpolations of the jump heights of the respective quantities at T_S (see supplement, Fig. S5). Table 1 summarizes the pressure dependence of the transition temperatures in CBSCl.

We find that both T_N and T_S are enhanced by hydrostatic pressure. Previous studies investigated the effects of chemical doping on the physical properties of CBSCl by substituting the lone-pair Bi site by Y[18] or lanthanide elements[19,21], exchanging the halide ion for Br or I[32], or Te doping the Se site[24]. Hydrostatic pressure applied to CBSCl was shown to enhance T_N by about 1 K/GPa[24] which is in line with our results. For the pressure dependence of T_S no literature data are available. The structural phase transition is absent in the compounds where Cl is exchanged for Br and I due to their larger ionic radii, and was not reported for any of the other doped versions of francisite.

Thermal Expansion for $\mathbf{B} > \mathbf{0}, \mathbf{B} \parallel \mathbf{c}$. The *c* axis is the easy-axis in CBSCl and shows a metamagnetic transition in magnetic fields $B \parallel c$, rendering it of special interest. Application of a magnetic field $B \parallel c$ suppresses the Néel transition to lower temperatures (Fig. 3b,c). Up to a field of 0.5 T an increase in the thermal expansion coefficient signals field-induced enhancement of the pressure dependence of the entropy changes ($\alpha_i \propto \partial S/\partial p_i$). At even higher fields the character of the phase transition changes from a continuous to a discontinuous transition. This change is evidenced by a broadening of the λ-like feature to a plateau-like behavior between two jumps (up and down) in α_c as the temperature is increased. A magnetic field of 1 T fully suppresses AFM order while a ferromagnetic phase appears. Notably, the exact same behavior described for α_c at low fields is also visible in the Fisher specific heat[33], $\partial(\chi_c T)/\partial T$, a derivative of the static magnetic susceptibility χ_c (Fig. 3a). This behavior and especially the intermediate phase emerging in an applied field will be discussed in more detail below.

Magnetostriction for $\boldsymbol{B \parallel c}$. Application of magnetic fields $B \parallel c$ drives the system into a ferromagnetic (FM) phase as indicated by sharp jumps in the magnetization (Fig. 4c,d). The metamagnetic transition is characterized by sharp jumps in the macroscopic length as seen in the magnetostriction measurements along the *c* axis (Fig. 4a,b). In both magnetization and length changes, a broad hysteresis region becomes visible upon ramping down the applied field at 2 K (0.86 T to 0.77 T), indicating the first-order nature of the transition. The FM state features the magnetization of $M_c = 0.87\ \mu_B$/Cu thereby indicating that the spins are not fully aligned but presumably canted. At 10 K and above a linear increase is visible in $dL_c(B)$ between a regime where $dL_c \approx 0$ at low fields and a constant value above the phase transition. The hysteresis region shrinks as the temperature is increased towards T_N and does not extend over the whole regime of linear increase.

Mixed-phase for $\mathbf{B} > \mathbf{0.4\ T}$. The linear increase and hysteresis observed in $dL_c(B, T < T_{\mathrm{crit}})$ points to a mixed phase between the low-field AFM ordered phase and the field-induced FM state. In this mixed intermediate phase both AFM and FM domains are present and the ratio FM:AFM linearly increases with the applied magnetic field, as the demagnetizing field is overcome and AFM regions align with the field. Such mixed-phase behavior is common for metamagnets and has also been observed in the brother compound $Cu_3Bi(SeO_3)_2O_2Br$[34]. There, the mixed-phase was found to exhibit broadband absorption with excitations extending over at least ten decades of frequency[34]. A similar behavior is naturally also expected in $Cu_3Bi(SeO_3)_2O_2Cl$.

Linear magnetoelastic coupling. On top of the mixed-phase behavior, a remarkable direct proportionality between the magnetization M_c and the relative length changes $dL_c(B)$, i.e., a linear magnetoelastic coupling $dL_c(M_c) = 9 \cdot 10^{-6} M_c$ [μ_B/Cu], is observed (Fig. 4) at $T < T_{\mathrm{crit}}$. A comparison of the jump heights at the metamagnetic transition, normalized to the jump heights at 2 K, illustrates this observation even more clearly (Fig. 5). The temperature evolution of both ΔM and ΔL_c are proportional to each other and obeys an order parameter-like behavior.[35], linear magnetostriction was first observed in CoF_2 by Borovik-Romanov and co-workers[36]. Among many others, antiferromagnetic examples include hematite (α-Fe_2O_3)[37], dysprosium orthoferrite[35] ($DyFeO_3$), and more recently the multiferroic $TbMnO_3$[38]. In all of these compounds linear magnetostriction is closely related to the presence of antiferromagnetic domains. The magnetic point group of CBSCl, $mm'm$, is not

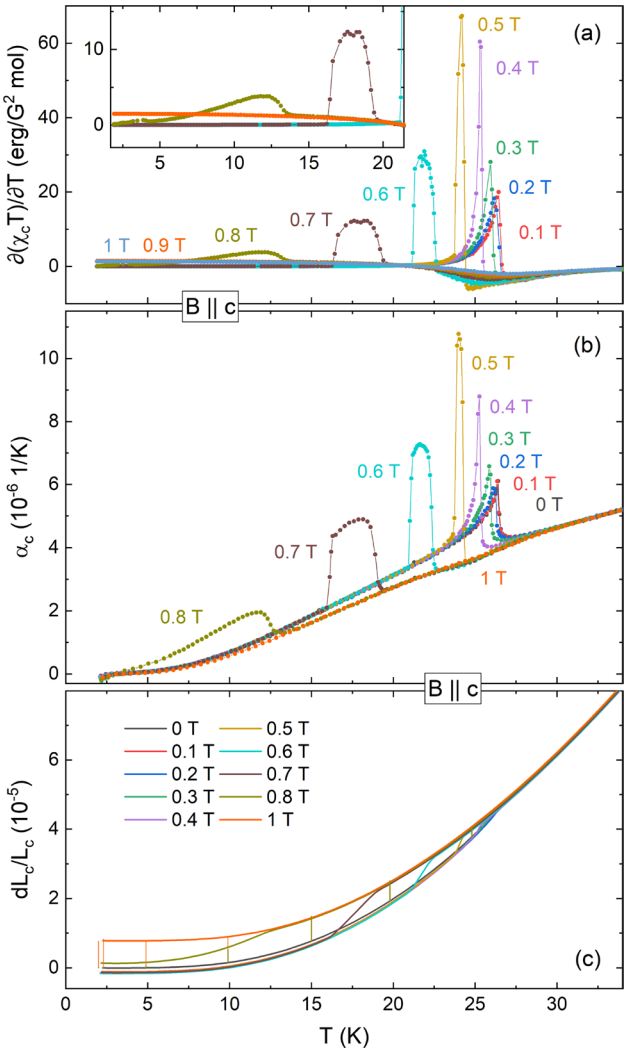

Figure 3. Fisher's specific heat and thermal expansion up to B = 1 T: (**a**) Fisher's specific heat calculated from the static magnetic susceptibility, (**b**) thermal expansion coefficient α_c, and (**c**) relative length changes, for $0\ \mathrm{T} \leq B \parallel c \leq 1\ \mathrm{T}$. The inset in (**a**) presents a magnification of the low temperature region. Vertical bars in (**c**) mark the relative length changes $\Delta L(B)$ from 0 T to 0.8 T (olive green) and 1 T (orange), respectively, obtained from magnetostriction measurements.

among the point groups in which a linear magnetostriction is expected to be dominant[39], which does not mean, however, that it may not, as observed, be dominant.

In addition to the linear magnetoelastic coupling, it was argued that the point group $mm'm$ is also compatible with a linear magnetoelectric coupling[25], and indeed, a linear magnetoelectric coupling was shown experimentally[24].

In-plane magnetic correlations far above $\mathbf{T_N}$. Thermal expansion measurements at 15 T reveal a large temperature regime above T_N where significant in-plane magnetostriction is present (see supplement, Fig. S7). Notably, magnetostriction along the c axis is negligible above T_N, whereas for the a and b axis there are pronounced magnetic field effects up to above 80 K. For the a axis the length changes are about one magnitude larger than for the b axis. Qualitatively, application of a magnetic field acts in the same way as the evolution of long-range order below T_N: the a axis shrinks whereas the b axis elongates. The strong difference between magnetostriction in the ab plane and along the c axis evidences strong in-plane magnetic correlations above T_N, in line with the large and competing FM and AFM exchange couplings on the order of 60 K to 70 K and the small interplane couplings on the order of up to 2 K[26,27]. Negligible magnetostriction along the out-of-plane direction, $\lambda_c = -\partial M_c/\partial p_c \sim \partial J/\partial p_c$ signals that the exchange interactions J are nearly independent of pressure $p \parallel c$.

Phase diagrams. The low-temperature magnetic phase diagrams for CBSCl as measured by thermal expansion (c axis) and magnetization (all axes) are presented in Fig. 6. Corresponding magnetization measurements are shown in the supplement (Fig. S9, S10, and S11). The saturation field of $B_{\mathrm{sat,a}} = 20.7(5)$ T is extrapolated from the data for $B \parallel a$, whereas $B_{\mathrm{sat,b}} = 7.1(2)$ T and $B_{\mathrm{sat,c}} = 0.86(2)$ T were obtained by measurements at 2 K

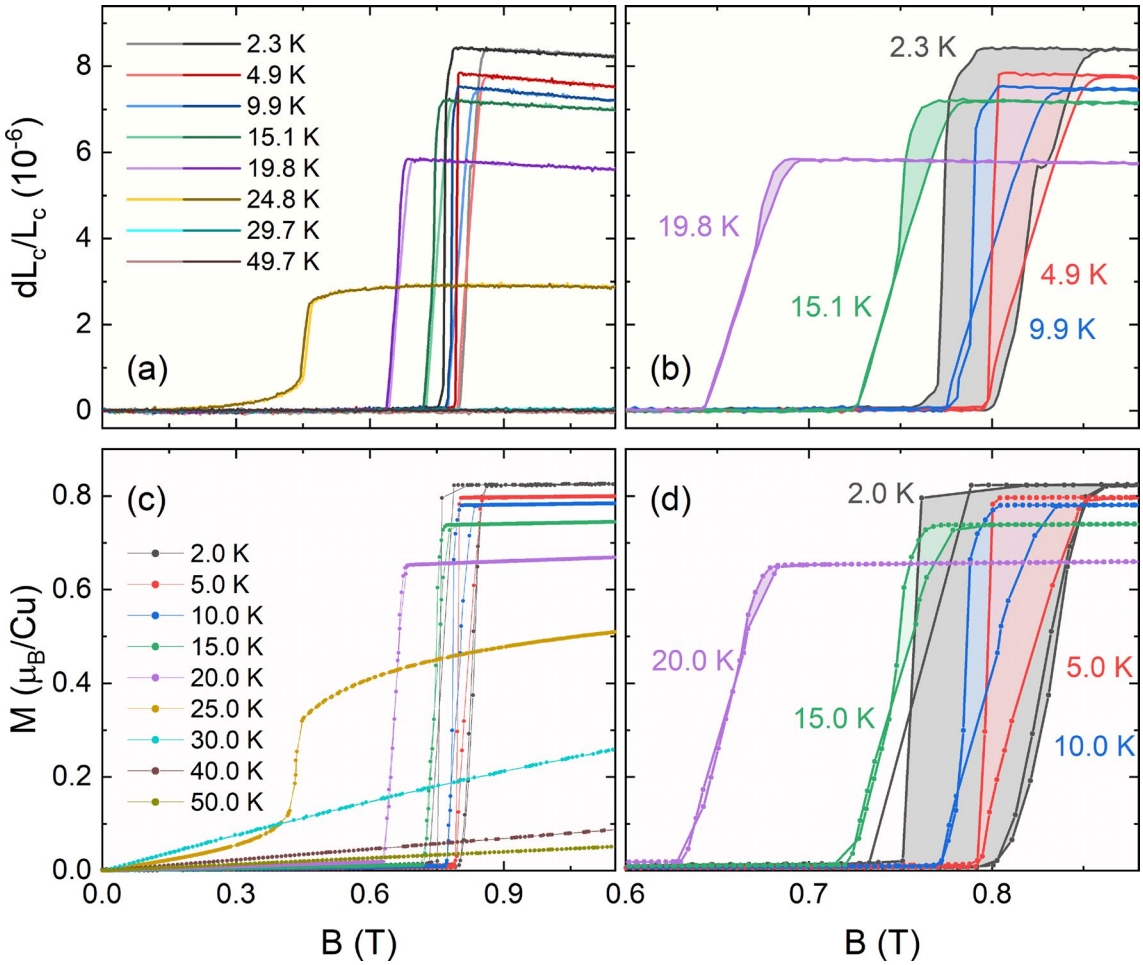

Figure 4. Linear magnetoelastic coupling: Magnetostriction and magnetization. Comparison of relative length changes $dL_c(B)/L_c(0)$ (**a**, **b**) and isothermal magnetization (**c**, **d**) for $B \parallel c$. Note that (**b**) and (**d**) show a magnification of the transition region and only data for selected temperatures. Hysteresis is marked by colored areas. Magnetostriction down-sweeps in (**b**) are shifted by 6 mT to correct for the remanent field of the magnet.

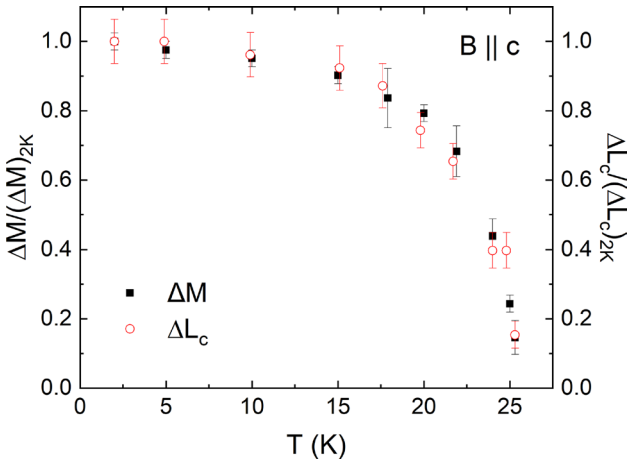

Figure 5. Linear magnetoelastic coupling: Jump sizes. Comparison of the jumps in magnetization (left ordinate) and relative length changes (right ordinate) at the metamagnetic transition normalized by their value at 2 K.

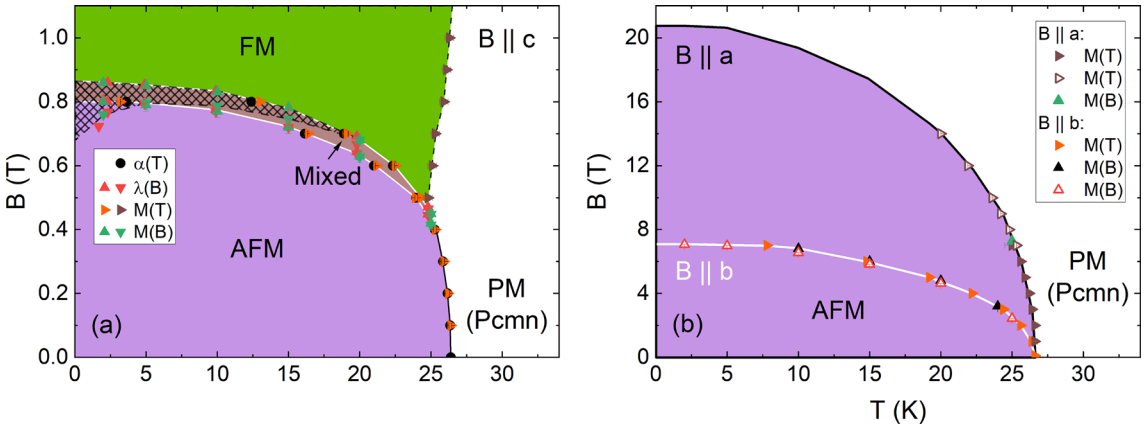

Figure 6. Magnetic Phase Diagrams: (**a**) Low-temperature magnetic phase diagram for $B \parallel c$. The hatched area displays the hysteresis region visible in isothermal magnetization and magnetostriction curves. Where hysteresis and the mixed phase overlap, white lines indicate phase boundaries obtained from up-sweep data. (**b**) Low-temperature magnetic phase diagram for $B \parallel a$ (black boundary) and $B \parallel b$ (white boundary) constructed from magnetization measurements. The phase boundary $T_N(B \parallel a > 14\,\mathrm{T})$ is obtained by scaling $T_N(B \parallel b)$.

for $B \parallel b$ and $B \parallel c$, respectively. For the c axis, a change in behavior from a continuous phase transition at zero- and low fields to a discontinuous transition above 0.4 T signals the presence of a tricritical point around 0.4 T. Moreover, a large magnetic field hysteresis at the metamagnetic transition is visible at low temperatures, which decreases as the temperature is increased.

Quantitative analysis of the phase boundaries for $\mathbf{B} \parallel \mathbf{c}$. By measuring the jump-like discontinuities in the magnetization and length at the metamagnetic phase boundary $B_{\mathrm{crit}}(T)$, the uniaxial pressure dependencies of the critical field and the critical temperature can be derived from the Clausius-Clapeyron equation and related thermodynamic equations[30]

$$\left(\frac{\partial T_{\mathrm{crit}}}{\partial p_c}\right)_B = V_{\mathrm{m}} \frac{\frac{\Delta L_c}{L_c}}{\Delta S} \tag{2}$$

$$\left(\frac{\partial T_{\mathrm{crit}}}{\partial B_c}\right)_p = -\frac{\Delta m_c}{\Delta S} = -\frac{\Delta (M_c \cdot V)}{\Delta S} \tag{3}$$

$$\left(\frac{\partial B_{\mathrm{crit}}}{\partial p_c}\right)_T = V_{\mathrm{m}} \frac{\frac{\Delta L_c}{L_c}}{\Delta m_c} \tag{4}$$

where $\Delta L_c/L_c$ and Δm_c are the observed jumps in the length and the magnetic moment. $\partial T_{\mathrm{crit}}/\partial B_c$ is calculated from two polynomial fits in different temperature regimes to the phase boundary $B_{\mathrm{crit}}(T)$ such that the changes in entropy, ΔS, can be calculated from Eq. (3). The pressure dependence of the critical field B_{crit} is small and positive, on the order of 80(6) mT/GPa at all temperatures. Derived changes of the transition temperature $T_{\mathrm{crit}}(B)$ at the metamagentic (AFM to FM) phase transition under pressure are large at low temperatures ($\partial T_{\mathrm{crit}}/\partial p_c = 34(16)$ K/GPa at 2 K) and decrease strongly as the temperature is increased ($\partial T_{\mathrm{crit}}/\partial p_c = 1.1(5)$ K/GPa at 24 K). Correspondingly, the entropy related to the phase transition increases from 30 mJ/(mol K) at 2 K to 360(130) mJ/(mol K) at 24 K. This analysis shows that uniaxial pressure $p \parallel c$ changes the exchange couplings in such a way that the AFM phase is stabilized with respect to both the FM and the paramagnetic (PM) phase. An overview of calculated values is given in the supplement in Table S2.

Critical scaling. In the vicinity of a critical point the specific heat is expected to behave as

$$c_{\mathrm{p}} = A \cdot t^{-\alpha} + B \qquad T > T_{\mathrm{crit}}$$
$$c_{\mathrm{p}} = A' \cdot |t|^{-\alpha'} + B' \qquad T < T_{\mathrm{crit}}$$

where $t = T/T_{\mathrm{crit}} - 1$ is the reduced temperature[40]. As seen in the Grüneisen scaling in Fig. 2, the magnetic contributions to the specific heat and the thermal expansion around T_N can be scaled to each other. Therefore, we can safely assume that a critical scaling of $\alpha_{i,\mathrm{mag}}$ close to T_N, i.e., above the shoulder-like feature at low temperatures ($t < -0.2$ for $i = a, b$ and $t < -0.06$ for $i = c$), with the expression from Eq. (5) is allowed. Although we use the magnetic contributions, $c_{\mathrm{p,mag}}$ and $\alpha_{i,\mathrm{mag}}$, for the fitting, there is an uncertainty on the phonon background correction. Therefore, and to account for possible further contributions on top of the critical behavior, we initially used the canonical expression (similar to the one in Ref.[41])

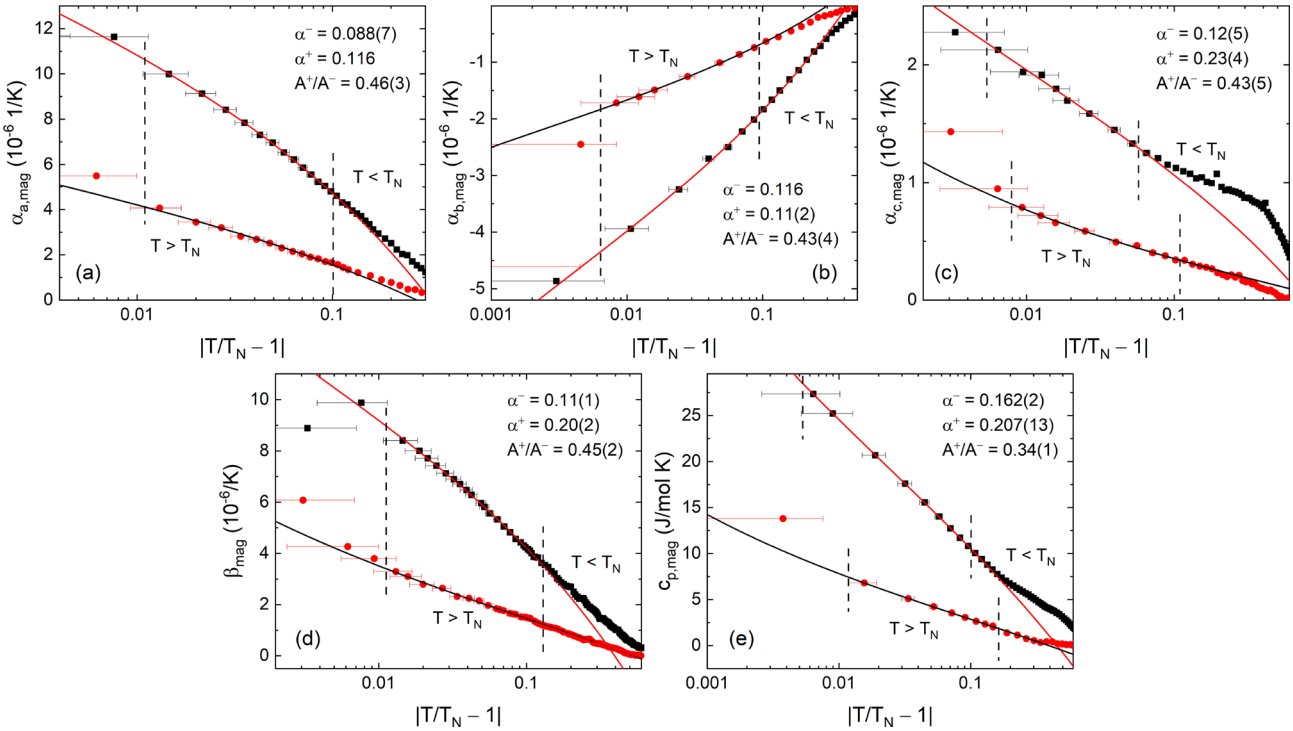

Figure 7. Critical scaling analysis near T_N. Semi-logarithmic plots of the magnetic contributions to (**a**–**c**) the thermal expansion coefficients $\alpha_{i,\mathrm{mag}}$, $i = a, b, c$, (**d**) the magnetic volume expansion coefficient β_{mag} and (**e**) the specific heat versus reduced temperature $|t| = |T/T_N - 1|$, for $T_N = 26.4$ K. Black squares (red circles) mark data for $T < T_N$ ($T > T_N$). Red and black solid lines are fits to the data according to Eq. (5), vertical dashed lines indicate the fitting window. Values for $\alpha^{\pm}$ with no error given were fixed for the fitting.

$$c_p = \frac{A^{\pm}}{\alpha^{\pm}}|t|^{-\alpha^{\pm}}(1 + E^{\pm}|t|^{0.5}) + B + D^{\pm}t \tag{5}$$

where "+" ("−") denotes fitting parameters for $T > T_{\mathrm{crit}}$ ($T < T_{\mathrm{crit}}$). It turned out, however, that the data can be fitted very well even when setting $B = 0$ and $D^{\pm} = 0$.

Depending on the critical exponent $\alpha^{\pm}$ and the ratio of the amplitudes, A^+/A^-, the critical behavior can be categorized by one of many universality classes. The most well-known universality classes for a d-dimensional lattice and an order parameter of dimensionality D are the 3D Heisenberg model ($d = 3, D = 3$), the 3D XY model ($d = 3, D = 2$), the 3D Ising model ($d = 3, D = 1$) and the 2D Ising model ($d = 2, D = 1$). Calculations for these different models predict $\alpha \approx -0.12$, $A^+/A^- \approx 1.5$ (3D Heisenberg), $\alpha \approx -0.01$, $A^+/A^- \approx 1$ (3D XY), $\alpha \approx 0.11$, $A^+/A^- \approx 0.5$ (3D Ising)[42], as well as $\alpha = 0$ (2D Ising)[43].

The fits to the critical region around T_N, roughly around $0.01 < |t| < 0.1$, for the linear thermal expansion coefficients, the volume expansion coefficient and the specific heat are shown in Fig. 7.S3). The two main results which stand out from the fits are that (1) the critical exponents $\alpha^{\pm}$ are all positive and lie between $\alpha^{\pm} = 0.088(7)$ and 0.23(4), and (2) the ratio of the amplitudes for $T > T_N$ and $T < T_N$, A^+/A^-, lies in the range from $A^+/A^- = 0.43(4)$ to 0.46(3) for the thermal expansion data, and $A^+/A^- = 0.34(1)$ for the specific heat. Considering these two main results, $\alpha^{\pm}$ values around 0.11 and ratios A^+/A^- close to 0.5 – but far away from 1 or even 1.5 – enables us to clearly categorize the transition around T_N as a transition with a one-dimensional order parameter on a three-dimensional lattice, i.e., a 3D Ising-type transition. This result is in line with the strong anisotropy visible in the magnetization and the phase diagrams of CBSCl as well as the strict (uniaxial) alignment of the Cu2 spins along the c axis.

Previous calculations successfully described many of the properties of $Cu_3Bi(SeO_3)O_2X$ (X = Cl,Br) by an effective 3D spin model, i.e., by Heisenberg spins combined with Dzyaloshinskii-Moriya (DM) interactions[26] and symmetric anisotropic exchange interactions[25]. Also, neutron diffraction measurements suggested that the direction of the Cu spins is constrained to the bc plane[25]. For the brother compound $Cu_3Bi(SeO_3)_2O_2Br$ (CBSBr), on the other hand, a crossover from a 2D XY ($\beta_c \leq 0.23$) to a 3D ($\beta_c = 0.30$) character was suggested from neutron diffraction measurements near $T_N = 27.4$ K[44]. Deviations from the critical behavior are also observed in our data below T_N, roughly for $t < -0.1$. Together with the observation of dispersionless magnon modes along the c direction at 2 K[25] this may point to 2D correlations evolving below T_N. However, whether or not the low-temperature behavior is caused by a 3D-to-2D crossover can not be concluded unambiguously from our data and necessitates further neutron or NMR studies. Therefore, while a crossover to a spatial 2D behavior as reported for CBSBr cannot be neither concluded nor excluded from our data on CBSCl, our results clearly point to a 3D Ising-like behavior in the critical region around T_N.

Conclusions

The buckled-kagomé antiferromagnet $Cu_3Bi(SeO_3)_2O_2Cl$ was investigated by thermal expansion, magnetostriction, magnetization and specific heat measurements. Its highly anisotropic lattice changes in temperature and in magnetic field reveal two phase transitions at $T_N = 26.4(3)$ K and $T_S = 120.7(5)$ K. The low-temperature and low-field AFM phase for $B \parallel c$, which experiences a field-driven metamagnetic transition to an FM phase, exhibits linear magnetoelastic coupling and a sizable mixed phase between the AFM and field-induced FM phases. Uniaxial pressure $p \parallel c$ stabilizes the AFM phase at the expense of the surrounding FM and paramagnetic (PM) phases. T_S is not affected by magnetic fields but strongly suppressed by uniaxial pressure along the in-plane directions, whereas $p \parallel c$ strongly enhances it by about 27 K/GPa. The critical behavior in the vicinity of T_N is in line with calculations for the 3D Ising model. Furthermore, while in-plane magnetic correlations extend to temperatures far above T_N the c axis shows no significant magnetostriction and effects of a magnetic field on the thermal expansion above T_N.

The francisite $Cu_3Bi(SeO_3)_2O_2Cl$ is an exciting compound with strong physical effects from both lattice and spin degrees of freedom at different temperatures. Our study provides additional evidence that the low-temperature phase of $Cu_3Bi(SeO_3)_2O_2Cl$ presents a versatile playground for investigating multiferroic effects, combining both a linear magnetoelastic and linear magnetoelectric coupling.

Methods

Crystal growth. Single crystals of $Cu_3Bi(SeO_3)_2O_2Cl$ were grown by the chemical vapor transport method as reported in Ref. [28]. Different single crystals of sizes $2.30 \times 1.80 \times 0.58$ mm^3 ($m = 7.76(5)$ mg), $1.0 \times 1.0 \times 0.12$ mm^3 ($m = 0.60(5)$ mg) and $2.50 \times 2.00 \times 0.60$ mm^3 ($m = 8.88(5)$ mg) were used for our studies.

High-resolution dilatometry. High-resolution capacitance dilatometry measurements were performed in two three-terminal high-resolution capacitance dilatometers from Kuechler Innovative Measurement Technology with a home-built setup placed inside a variable temperature insert of an Oxford magnet system[45,46]. Linear thermal expansion coefficients $\alpha_i = 1/L_i \times dL_i(T)/dT$ were derived for all crystallographic axes, i.e., $i = a, b, c$, in a temperature range from 2 K to 200 K, with magnetic fields up to 15 T applied along the measurement direction. Field-induced length changes $dL_i(B)$ were measured at various fixed temperatures between 1.7 K and 200 K and the magnetostriction coefficients $\lambda_i = 1/L_i \times dL_i(B_i)/dB_i$ were derived.

Magnetization. Magnetization measurements were performed in a Magnetic Properties Measurement System (MPMS3, Quantum Design) up to 7 T and in a Physical Property Measurement System (PPMS-14, Quantum Design) in fields up to 14 T. A rotatable sample holder was used in the MPMS3 for measurements perpendicular to the c axis in order to determine the a and b axis for further magnetization measurements. Laue XRD measurements confirmed the orientation and quality of the crystals (see supplement, Fig. S1).

Specific heat. Specific heat measurements were performed on a PPMS calorimeter using a relaxation method, on a sample of $m = 1.8$ mg.

Data availability

All data used in this study are available from the corresponding author upon reasonable request.

Received: 29 September 2021; Accepted: 22 April 2022
Published online: 05 May 2022

References

1. Lacroix, C., Mendels, P. & Mila, F. (eds.) *Introduction to Frustrated Magnetism, Springer Series in Solid-State Sciences* 1 edn, vol. 164 (Springer-Verlag Berlin Heidelberg, 2011).
2. Ramirez, A. P. Strongly geometrically frustrated magnets. *Ann. Rev. Mater. Sci.* **24**, 453–480 (1994).
3. Mendels, P. & Bert, F. Quantum kagome frustrated antiferromagnets: One route to quantum spin liquids. *Comptes Rendus Physique* **17**, 455–470 (2016). Physique de la matière condensée au XXIe siècle: l'héritage de Jacques Friedel.
4. Khomskii, D. I. *Transition Metal Compounds* (Cambridge University Press, 2014).
5. Savary, L. & Balents, L. Quantum spin liquids: a review. *Rep. Progress Phys.* **80**, 016502 (2016).
6. Pregelj, M. *et al.* Multiferroicity in the geometrically frustrated $FeTe_2$ O_5 Cl. *Phys. Rev. B* **88**, 224421 (2013).
7. Yoo, K. *et al.* Magnetic field-induced ferroelectricity in S = 1/2 kagome staircase compound PbCu3TeO7. *npj Quant. Mater.* **3**, 1–9 (2018).
8. Cabrera, I. *et al.* Coupled magnetic and ferroelectric domains in multiferroic Ni_3 V_2 O 8. *Phys. Rev. Lett.* **103**, 087201 (2009).
9. Zhang, Q. *et al.* Complex magnetoelastic properties in the frustrated kagome-staircase compounds $(Co_{1-x}Ni_x)_3V_2O_8$. *Phys. Rev. B* **84**, 184429 (2011).
10. Spaldin, N. A. & Fiebig, M. The renaissance of magnetoelectric multiferroics. *Science* **309**, 391–392 (2005).
11. Fiebig, M., Lottermoser, T., Meier, D. & Trassin, M. The evolution of multiferroics. *Nat. Rev. Mater.* **1**, 16046 (2016).
12. Manipatruni, S., Nikonov, D. E. & Young, I. A. Beyond CMOS computing with spin and polarization. *Nat. Phys.* **14**, 338–343 (2018).
13. Manipatruni, S. *et al.* Scalable energy-efficient magnetoelectric spin-orbit logic. *Nature* **565**, 35–42 (2019).
14. Bibes, M. & Barthélémy, A. Towards a magnetoelectric memory. *Nat. Mater.* **7**, 425–426 (2008).
15. Liu, M. & Sun, N. X. Voltage control of magnetism in multiferroic heterostructures. *Philos. Trans. Royal Soc. A: Math., Phys. Eng. Sci.* **372**, 20120439 (2014).
16. Spaldin, N. A. & Ramesh, R. Advances in magnetoelectric multiferroics. *Nat. Mater.* **18**, 203–212 (2019).
17. Becker, R. & Johnsson, M. Crystal structure of Cu_3 Bi ($TeO_3)_2$ O_2 Cl: A Kagomé lattice type compound. *Solid State Sci.* **7**, 375–380 (2005).

18. Zakharov, K. V. *et al.* Thermodynamic properties, electron spin resonance, and underlying spin model in Cu_3 Y ($SeO_3)_2$ O_2 Cl. *Phys. Rev. B* **90**, 214417 (2014).
19. Zakharov, K. V. *et al.* Magnetic, resonance, and optical properties of Cu_3 Sm ($SeO_3)_2$ O_2 Cl: A rare-earth francisite compound. *Phys. Rev. B* **94**, 054401 (2016).
20. Klimin, S. A. & Budkin, I. V. Magnetic phase transitions in two-dimensional frustrated Cu_3 R ($SeO_3)_2$ O_2 Cl. *Spectr. Study. EPJ Web of Conf.* **132**, 2016–2017 (2017).
21. Markina, M. M. *et al.* Interplay of rare-earth and transition-metal subsystems in Cu_3 Yb ($SeO_3)_2$ O_2 Cl. *Phys. Rev. B* **96**, 134422 (2017).
22. Markina, M. *et al.* Francisites as new geometrically frustrated quasi-two-dimensional magnets. *Physics-Uspekhi* **64**, 344–356 (2021).
23. Pring, A., Gatehouse, B. M. & Birch, W. D. Francisite, Cu_3 Bi ($SeO_3)_2$ O_2 Cl, a new mineral from Iron Monarch, South Australia; description and crystal structure. *Am. Miner.* **75**, 1421–1425 (1990).
24. Wu, H. C. *et al.* Anisotropic pressure effects on the kagome Cu_3 Bi ($SeO_3)_2$ O_2 Cl metamagnet. *J. Phys. D: Appl. Phys.* **50**, 265002 (2017).
25. Constable, E. *et al.* Magnetic and dielectric order in the kagomelike francisite Cu_3 Bi ($SeO_3)_2$ O_2 Cl. *Phys. Rev. B* **96**, 014413 (2017).
26. Rousochatzakis, I., Richter, J., Zinke, R. & Tsirlin, A. A. Frustration and dzyaloshinsky-moriya anisotropy in the kagome francisites Cu_3 Bi ($SeO_3)_2$ O_2 X (X = Br, Cl). *Phys. Rev. B* **91**, 024416 (2015).
27. Nikolaev, S. A., Mazurenko, V. V., Tsirlin, A. A. & Mazurenko, V. G. First-principles study of the magnetic ground state and magnetization process of the kagome francisites Cu_3 Bi ($SeO_3)_2$ O_2 X (X = Cl, Br). *Phys. Rev. B* **94**, 144412 (2016).
28. Gnezdilov, V. *et al.* Lattice and magnetic instabilities in Cu_3 Bi ($SeO_3)_2$ O_2 X (X = Br, Cl). *Phys. Rev. B* **96**, 115144 (2017).
29. Milesi-Brault, C. *et al.* Archetypal soft-mode-driven antipolar transition in francisite Cu_3 Bi ($SeO_3)_2$ O_2 Cl. *Phys. Rev. Lett.* **124**, 097603 (2020).
30. Barron, T. H. K. & White, G. K. *Heat Capacity and Thermal Expansion at Low Temperatures*. The International Cryogenic Monograph Series (Kluwer Academic / Plenum Publishers, 1999).
31. Klingeler, R., Büchner, B., Cheong, S.-W. & Hücker, M. Weak ferromagnetic spin and charge stripe order in $La_{5/3}$ $Sr_{1/3}$ NiO_4. *Phys. Rev. B* **72**, 104424 (2005).
32. Millet, P. *et al.* Syntheses, crystal structures and magnetic properties of francisite compounds CuBi ($SeO_3)_2$ O_2 X (X = Cl, Br and I). *J. Mater. Chem.* **11**, 1152–1157 (2001).
33. Fisher, M. E. Relation between the specific heat and susceptibility of an antiferromagnet. *Philos. Mag.: J. Theor. Exp. Appl. Phys.* **7**, 1731–1743 (1962).
34. Pregelj, M. *et al.* Controllable broadband absorption in the mixed phase of metamagnets. *Adv. Funct. Mater.* **25**, 3634–3640 (2015).
35. Zvezdin, A. K. *et al.* Linear magnetostriction and the antiferromagnetic domain structure in dysprosium orthoferrite. *Zhurnal Eksperimental'noi i Teoreticheskoi Fiziki* **88**, 1098–1102 (1985).
36. Borovik-Romanov, B. E., Javelov A. S, Physics and techniques of low temperatures. *Proc. 3rd Regional Conf. Prague* (1963).
37. Scott, R. A. M. & Anderson, J. C. Indirect observation of antiferromagnetic domains by linear magnetostriction. *J. Appl. Phys.* **37**, 234–237 (1966).
38. Aliouane, N. *et al.* Field-induced linear magnetoelastic coupling in multiferroic $TbMnO_3$. *Phys. Rev. B* **73**, 020102 (2006).
39. Birss, R. R. & Anderson, J. C. Linear magnetostriction in antiferromagnetics. *Proc. Phys. Soc.* **81**, 1139–1140 (1963).
40. Kadanoff, L. P. *et al.* Static phenomena near critical points: Theory and experiment. *Rev. Mod. Phys.* **39**, 395–431 (1967).
41. Kornblit, A. & Ahlers, G. Heat capacity of $RbMnF_3$ near the antiferromagnetic transition temperature. *Phys. Rev. B* **8**, 5163–5174 (1973).
42. Pelissetto, A. & Vicari, E. Critical phenomena and renormalization-group theory. *Phys. Rep.* **368**, 549–727 (2002).
43. Le Guillou, J. C. & Zinn-Justin, J. Critical exponents from field theory. *Phys. Rev. B* **21**, 3976–3998 (1980).
44. Pregelj, M. *et al.* Magnetic ground state and two-dimensional behavior in pseudo-kagome layered system CuBi ($SeO_3)_2$ O_2 Br. *Phys. Rev. B* **86**, 144409 (2012).
45. Küchler, R. *et al.* The world's smallest capacitive dilatometer, for high-resolution thermal expansion and magnetostriction in high magnetic fields. *Rev. Sci. Instrum.* **88**, 083903 (2017).
46. Werner, J. *et al.* Anisotropy-governed competition of magnetic phases in the honeycomb quantum magnet Na_3 Ni_2 SbO_6 studied by dilatometry and high-frequency esr. *Phys. Rev. B* **95**, 214414 (2017).

Acknowledgements

We acknowledge financial support by BMBF via the project SpinFun (13XP5088) and by Deutsche Forschungsgemeinschaft (DFG) under Germany's Excellence Strategy EXC2181/1-390900948 (the Heidelberg STRUCTURES Excellence Cluster) and through project KL 1824/13-1. For the publication fee we acknowledge financial support by DFG within the funding programme "Open Access Publikationskosten" as well as by Heidelberg University. Support by the P220 program of the Government of Russia through the project 075-15-2021-604 is acknowledged. MM acknowledges support by the Russian Foundation for Basic Research through grant 20-02-00015.

Author contributions

S.Sp. performed dilatometry, Laue x-ray diffraction, and magnetization measurements together with their analysis. P.B., M.M., and A.V. synthesized and characterized the single crystals. M.M. performed specific heat measurements. S.Sp. wrote the draft. R.K. supervised the project. All authors reviewed and commented on the manuscript.

Funding

Open Access funding enabled and organized by Projekt DEAL.

Competing Interests

The authors declare no competing interests.

Additional information

Supplementary Information The online version contains supplementary material available at https://doi.org/10.1038/s41598-022-11368-5.

Correspondence and requests for materials should be addressed to S.S.